# Using ultrasound imaging to identify flow reattachment in shear-thinning suspensions

M. Barnes[1*], G. Rosi[1,2], F. Kaiser[3], D. Rival[1,2]

1: Dept. of Mechanical & Materials Engineering, Queen's University, Canada
2: Inst. of Fluid Mechanics, Technische Universität Braunschweig, Germany
3: RheEnergise Ltd., Montreal, Canada
*Corresponding author: moira.barnes@queensu.ca

**Keywords:** Ultrasound Imaging, Suspensions, Expansion Flows, Reattachment.

## ABSTRACT

The current study explores ultrasound imaging velocimetry (UIV) as an alternative method for capturing flow fields in shear-thinning suspensions. In particular, UIV is used here together with pressure measurements to identify the reattachment point and to correlate the point's location with the pressure recovery downstream of an axisymmetric expansion. Four fluids are investigated: pure water, as well as three 1750ppm xanthum-gum-in-water solutions mixed with non-reactive mineral micro-particles at 0%, 15% and 30% volume fractions. Wall-pressure measurements were collected through taps located at 0 to 13 throat diameters downstream of the expansion with subsequent UIV measurements collected from 0.5 to 5 throat diameters downstream of the expansion. Pressure-tap measurements for the tested suspensions demonstrate $80\%$ to $100\%$ total pressure recovery achieved at approximately 4 to 5 throat diameters downstream from the throat. Furthermore, all four fluids exhibit total pressure recoveries within 10% of Borda-Carnot prediction. Despite similar pressure recoveries, UIV revealed different reattachment lengths for the tested fluids. Water exhibited a reattachment length of approximately four throat diameters, which is expected within the tested turbulent regime, while the xanthum-gum solution exhibited a delayed reattachment beyond the field-of-view when the effective Reynolds number is $O(10^2)$. Pipe-wall velocity measurements suggest that the dense suspensions exhibit similar reattachment lengths to that of water despite expectations that the dense suspensions would behave similar to the pure xanthum-gum solution given: the similar Reynolds number between the pure xanthum-gum solution and the tested dense suspensions; and previous work done by Barnes et al. (2024) and others revealing shear-layer stabilization within dense suspensions. It is suspected that increased diffusion within the suspension mitigates the shear layer's ability to convect downstream, but improved measurements are required to state this conclusively.

## 1. Introduction

At first glance, flows involving suspensions in shear-thinning fluids (STS flows) would appear relevant to a very narrow class of applications. However, such flows have become increasingly relevant to critical areas of research. Besides more typical examples found in the petrochemical and foodstuff industries (Brennen, 2005), STS flows are central in the development of novel research.

For example, the motions of cells or micro-organisms within shear-thinning fluids like mucus or blood can be classified as a STS flow (Pedley & Kessler, 1992). Understanding the motions of particles within STS flows is crucial in the development of technologies for sorting target particles or cells in various biological and pharmaceutical processes (Raihan et al., 2020). STS flows are also relevant towards understanding the electrochemical properties of certain dense suspensions, which is significant in developing improved energy storage methods (Kupsch et al., 2021).

It is becoming increasingly crucial to capture entire flow fields of processes involving STS flows, given their relevance to various ongoing research. However, standard optical methods face several challenges when measuring in this environment. The opacity of some STS flows makes it extremely difficult to either illuminate volumes or capture the motions of tracer particles (Deen et al., 2002). Even in experiments where the opacity has been alleviated using index matching of the dispersed phase, or through the florescence of tracer particles, standard methods still face challenges such as light scattering and refractive-index mismatching that ultimately reduce the signal-to-noise ratio and the achievable particle-per-pixel density of the measurement (Zhang & Rival, 2018).

The challenges faced by standard optical methods have given rise to alternative velocimetry measurement techniques that do not require unobstructed optical access. Current state-of-the-art methods include magnetic resonance velocimetry (MRV) (Elkins & Alley, 2007) or x-ray velocimetry (Mäkiharju et al., 2022), both of which are unobstructed by the presence of a disperse phase. Ultrasonic Imaging Velocimetry (UIV) also shares in the same benefits, but avoids challenges such as: affordability, complex post-processing and test facilities devoid of ferromagnetic materials as faced by MRV; or regulatory issues and the complexity surrounding disentangling the integrated measurement along the beam axis as faced by x-ray velocimetry (Poelma, 2016). UIV has been successfully employed towards the investigation of various dense suspensions. Example include: Kupsch et al. (2021), who investigated narrow-channel flows found within operational zinc-air batteries, revealing a flat-top velocity profile and increased wall-slip; Han et al. (2019), who investigated "particle jamming" phenomena in dense suspensions upon solid impact; and Crapper et al. (1998) who demonstrated the suitability of UIV towards studying sediment flows relevant to oceanography and ocean engineering. A thorough review of UIV along with additional examples can be found in Poelma (2016).

The current study seeks to push the limits of UIV by measuring in dense-suspension flows with volume fractions not yet attempted. Specifically, UIV is applied in concert with pressure measurements to identify the reattachment point downstream of a sudden axisymmetric expansion of a STS fluid, and to investigate the point's correlation with the fluid's pressure recovery. The following section describes the experimental setup, including the tested fluids, the test facility and the expansion, the pressure measurements, and the UIV apparatus. Results are then discussed, which include the pressure-recovery measurements for all tested fluids, imaging data gathered via the UIV setup, and flow fields and reattachment lengths as determined through the UIV. Finally, the implications of the results as it pertains to reattachment length and pressure recovery are summarized, and the successes and limitations of UIV in measuring the tested fluids are discussed.

## 2. Methods

The following section first describes the flow-loop facility and the geometry of the sudden expansion. The pressure sensors and their locations along the expansion are then described, as well as the UIV apparatus and its resultant field-of-view. The properties of the four fluids tested within the sudden expansion are then presented. Finally, the test matrix of the measurement campaign is laid out in terms of the volume fraction of the disperse phase, and in terms of the throat velocity, which is presented nominally and in terms of an equivalent Reynolds number described herein.

### 2.1. Properties of Tested Fluids

Pressure and UIV measurements were taken in water, as well as in three 1750 parts-per-million xanthan-gum-in-water solutions mixed with insoluble non-reactive mineral micro-particles ($\rho_p > 4000\mathrm{kg/m^3}$) to form suspensions with particle-volume fractions of $\Phi = 0\%$, $15\%$, and $30\%$, respectively. For brevity, these four fluids will be respectively referred to as water, XG$\Phi$0%, XG$\Phi$15%, and XG$\Phi$30%. Fig. 1(a) shows the particle-size distribution of three independent samples that were assessed using a Horiba Partica Laser Scattering Particle Size Distribution Analyzer LA-950V2. The small particle size in combination with the dissolved viscosifier (xanthan gum) lead to small Stokes numbers and avoided settling of the suspensions in between experiments. The fluids were weighed to determine their density ($\rho$). An Anton Paar MCR302 Rheometer was used to characterize the viscosity of the fluids. Fig. 1(b) shows the viscosity as a function of the shear rate for XG$\Phi$0%, XG$\Phi$15%, and XG$\Phi$30%, respectively. Until the onset of a Taylor-Couette instability in the Rheometer's cylinder-cup geometry (marked as dashed-dotted lines in Fig. 1(b)) the data can be described by power-law coefficients in the form $\mu = K\dot{\gamma}^{(n-1)}$ (dashed lines), where $\dot{\gamma}$ is the shear rate. Increasing the volume fraction of solids has little impact on the shear-thinning behaviour (slope $n \approx$ const). However, an increased $K$ leads to an upward shift of the viscosity curves for denser suspensions. Fluid properties were ultimately used to calculate the effective Reynolds number $\mathrm{Re_{eff}} = \rho U_t d / \mu_{\mathrm{eff}}$, where $\dot{\gamma} = 2U_t/(D-d)$ was used to calculate $\mu_{\mathrm{eff}}$, and the static pressure coefficient $\sigma = \Delta p/(0.5\rho U_t^2)$. An overview of the fluid properties is provided in Table 1.

| Fluid | $\rho\ (\mathrm{kg/m^3})$ | $K\,(\mathrm{mPa\cdot s^n})$ | $n$ (unitless) |
|---|---|---|---|
| Water | 998 | 0.89 | 1.000 |
| XG$\Phi$0% | 998 | 322.9 | 0.369 |
| XG$\Phi$15% | 1450 | 559.0 | 0.365 |
| XG$\Phi$30% | 1955 | 832.4 | 0.390 |

**Table 1.** Densities and rheological properties of tested fluids.
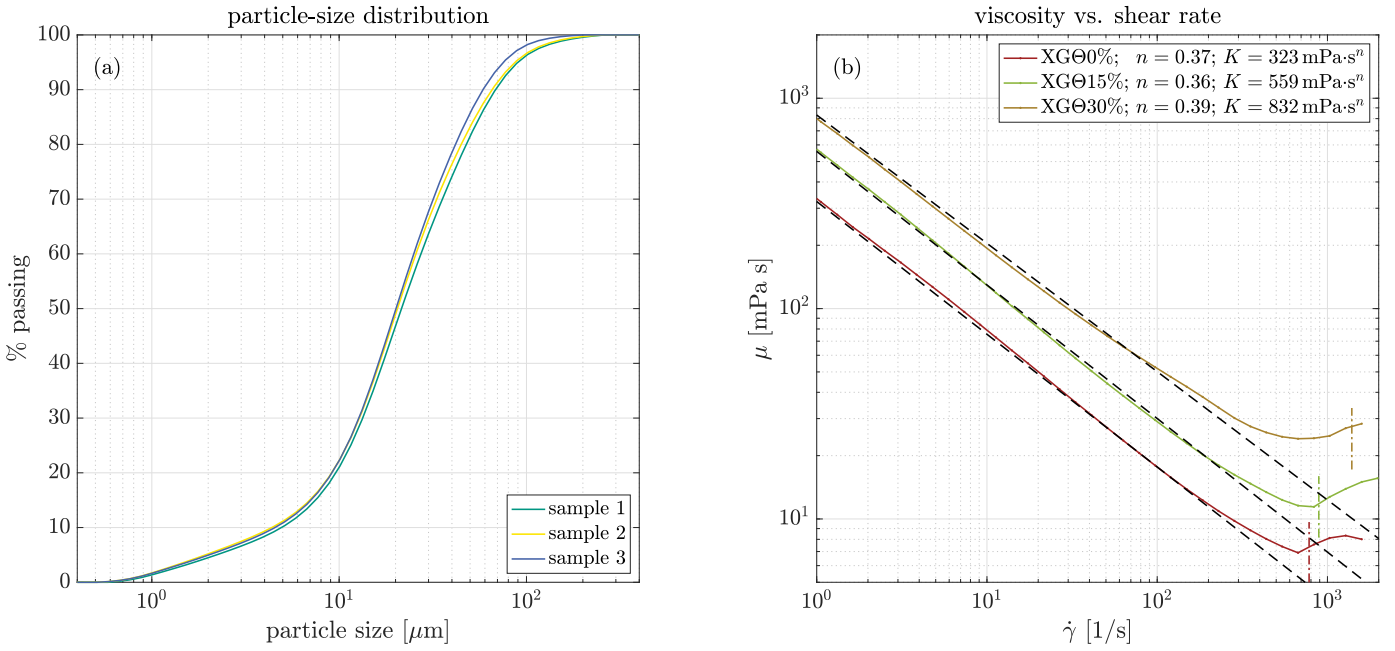
**Figure 1.** (a) Particle-size distribution of the mineral particles in the dense suspension; and (b) viscosity curves of the shear-thinning fluids XGΦ0%, XGΦ15%, and XGΦ30%.

## 2.2. Flow Loop Facility

Measurements were performed in RheEnergise's HTC2.0 facility within the Low-Pressure-Flow-Loop (XLPFL). The flow loop is shown in Fig. 2(a). The loop is constructed primarily out of 101.6mm tubing and circulates fluid using a KSB ETL 100-100-200 inline pump. Flow rates are recorded by an ABB (FSM4000) flow meter, while density measurements were periodically performed via an inline Promass I-300 Coriolis flowmeter. Pressure and UIV measurements were captured within the test section shown schematically in Fig. 2(b). The test section comprised of an axisymmetric expansion with a throat diameter ($d$) of 36.4mm and a pipe diameter ($D$) of 72.8mm resulting in a diameter ratio of $\beta = 0.5$. The throat of the expansion is located $27.2d$ downstream from the inlet of the test section, while the outlet of the test section is located $23.0d$ downstream from the expansion's throat. The contraction occurs gradually over a distance of a single throat diameter, the profile of which is provided as an equation in Fig. 2(b). Pressure taps (Omega PX419, 0.08% accuracy, vacuum, range: 0 to -6.894kPa) were placed at one location upstream of the throat, as well as six positions downstream of the throat as indicated in Fig. 2(b), from which the static-pressure coefficient $\sigma = \Delta p/(0.5\rho U_t^2)$ was calculated. Here, $U_t$ refers to the mean velocity at the expansion's throat, while $\Delta p$ is the difference between the downstream pressure and the throat pressure. UIV measurements were taken via a GE Healthcare L14-5/38 linear probe with 128 elements and a 0.3mm pixel pitch, coupled with a Vantage 128 ultrasound system from Verasonics. The Vantage system allows for plane wave imaging by simultaneously activating all elements within the ultrasound probe, thereby achieving high temporal resolutions. Tilted plane wave imaging was used to improve image quality, and ultimately resulted in a spatial resolution of 0.75mm-by-0.75mm per pixel. The field-of-view captured by the ultrasonic probe spanned a
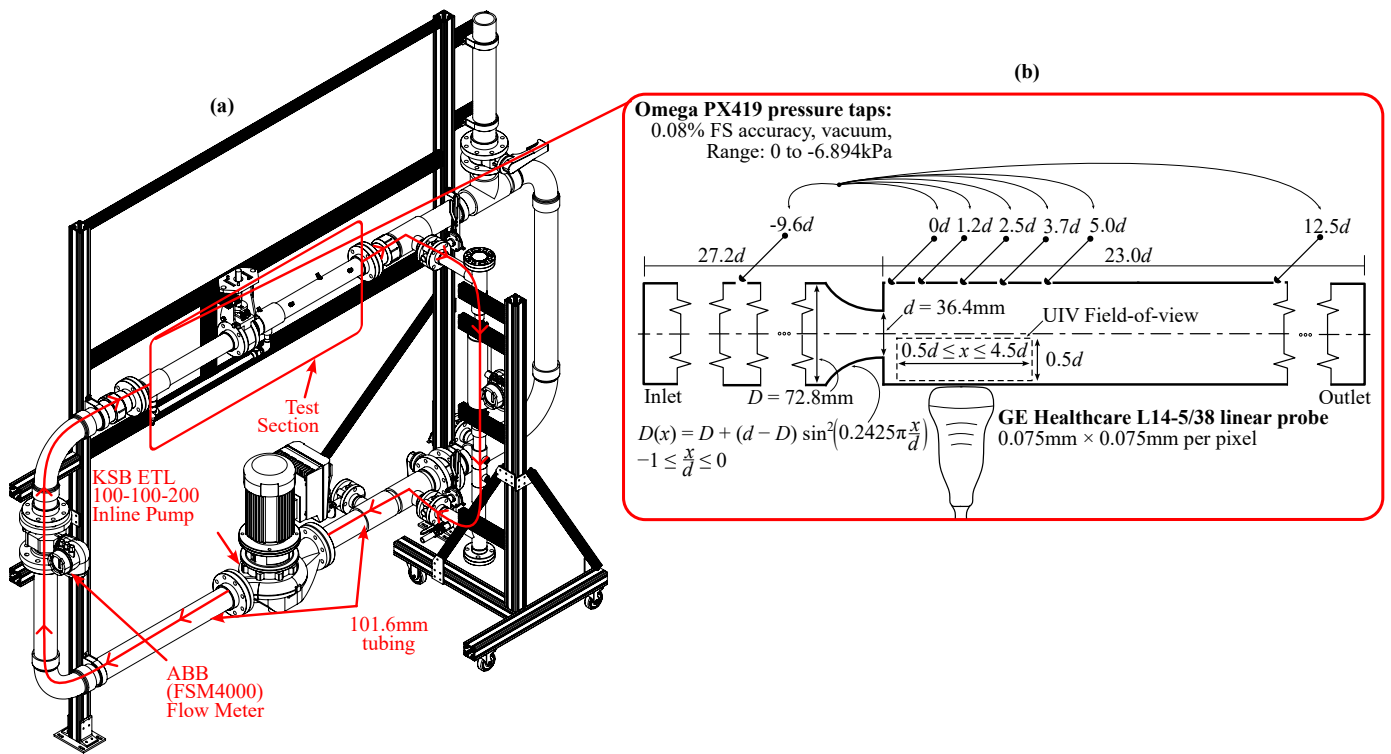
**Figure 2.** (a) Schematic of the Low-Pressure-Flow-Loop (XLPFL) facility with the locations of the pump, flow meter and test section indicated. (b) Schematic of the test section with relevant geometry, locations of pressure taps, and the UIV field-of-view indicated.

distance of $1d$ in the streamwise direction and $1.2d$ in the radial direction. Through repositioning the the ultrasound probe at $x/d = 1.5, 2.5$ and $3.5$, measurements spanning a streamwise domain of $0 \leq x/d \leq 4.5$ were possible.

For measurements involving water, $10\mu$m-diameter contrast-agent bubbles were seeded into the flow as tracer particles, while for measurements involving XG$\Phi$0%, air bubbles were used as tracer particles. Both tracers exhibited a Stokes number far beneath unity during all experiments, ensuring tracer accuracy errors less than 1%. Lastly, for cases involving XG$\Phi$15% and XG$\Phi$30%, the mineral particles functioned as tracer particles. At worst, the Stokes number of the mineral particles roughly equals unity, corresponding to tracer accuracy errors of approximately 1%.

## 2.3. Test Matrix

The test matrix of the measurement campaign is summarized in Table 2. The leftmost column presents tested fluids, while the second and third columns present the nominal throat velocity and the throat velocity normalized as the effective Reynolds number, respectively. Pressure measurements were taken for all listed cases. However, UIV measurements were attempted only for the boldfaced cases.

| Fluid | Throat Velocities (m/s) | $\mathrm{Re_{eff}}/10^3$ |
|-------|------------------------|--------------------------|
| Water | **0.51**, 1.01, **1.52**, 3.00, 4.52 | **20.6**, 41.3, **61.9**, 122.6, 184.7 |
| XG$\Phi$0% | **0.51**, 1.01, **1.52**, 3.00, 4.52 | **0.46**, 1.43, **2.8**, 8.5, 16.6 |
| XG$\Phi$15% | **0.51**, 1.01, **1.52**, 3.00, 4.52 | **0.40**, 1.2, **2.4**, 7.2, 14.1 |
| XG$\Phi$30% | **0.51**, 1.01, **1.52**, 3.00 | **0.33**, 1.0, **1.9**, 5.7 |

**Table 2.** Test matrix summary.

## 3. Pressure Recovery Downstream of the Expansion

Fig. 3 presents the static-pressure coefficient $\sigma = \Delta p/(0.5\rho U_t^2)$ for all four fluids. The pressure recoveries for all four fluids agree with the Borda-Carnot prediction of $\sigma = 2\beta^2(1 - \beta^2)$, regardless of composition or effective Reynolds number. Furthermore, regardless of effective Reynolds number or composition, all four fluids exhibit similar trends in pressure recovery. Specifically, all four fluids exhibit little pressure recovery prior to a single throat diameter downstream. This is followed by a rapid increase in pressure recovery that culminates to roughly 80% of the Borda-Carnot prediction within five throat diameters. Lastly, the pressure recovery asymptotes towards the Borda-Carnot prediction moving further downstream from the throat. Similar results were observed by Escudier & Smith (1999), who measured the pressure recovery downstream of an axisymmetric expansion for water and 2000 parts-per-million xanthum-gum-in-water solution, but not for STSs as tested here. Fig. 4 presents the total static-pressure recovery coefficient as a function of the effective Reynolds number for all test cases. Besides two outliers, all cases fall within 10% of the Borda-Carnot prediction, and exhibit no meaningful trends with the effective Reynolds number or fluid type. Tashiro & Tomita (1984, 1986) also observed strong agreement with the Borda-Carnot prediction across a variety of different flow conditions for air-solid suspensions.

The results presented herein would suggest that neither the disperse phase nor the shear-thinning nature of the continuous phase have an effect on the pressure recovery downstream of the expansion. If the pressure recovery is in fact unaffected, one might also expect a consistent flow topology across all four tested fluids, and by extension a similar reattachment point, which controls the rate of deceleration and consequentially the rate of pressure recovery. Towards identifying the reattachment point and correlating its position with pressure recovery, UIV data was collected. The following section describes the UIV data used to identify the reattachment point for all four fluids.

## 4. UIV Measurement Data

Ultrasound image data for the cases outlined in Table 2 were collected for all four fluids. Typical images for all fluids are shown in Fig. 5. For all four images, the pipe wall is located along the top edge and flow runs left to right. For both water and XG$\Phi$0%, the absence of a disperse phase results in very clear particle images that are amenable to flow-field measurements. However, for XG$\Phi$15% and XG$\Phi$30%, the presence of the disperse phase and trapped air causes the scattering and attenua-
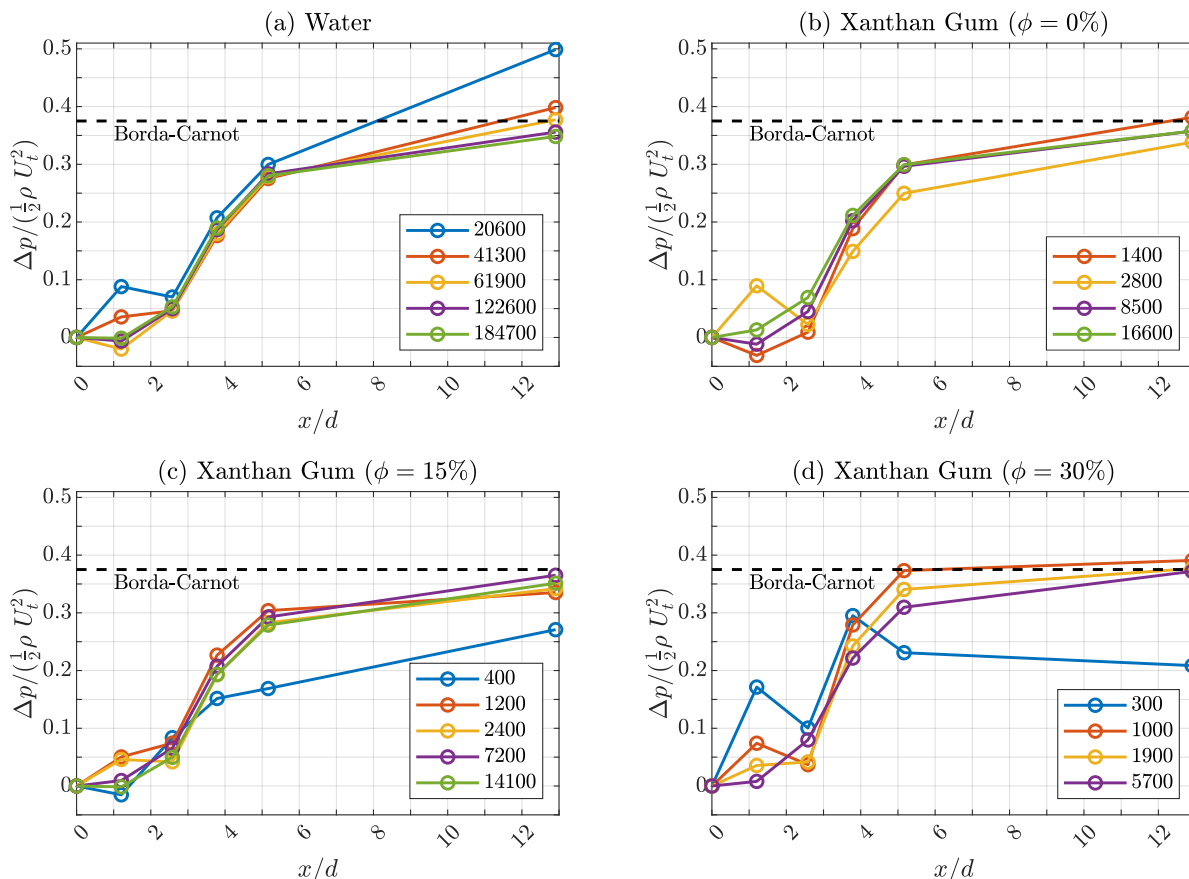
**Figure 3.** Pressure recovery coefficient ($\Delta p/(0.5\rho U_t^2)$) plotted against downstream distance from the expansion's throat, normalized by throat diameter ($x/d$), for (a) water, (b) XG$\Phi$0%, (c) XG$\Phi$15% and (d) XG$\Phi$30%. The legend presents throat velocities in terms of $\mathrm{Re_{eff}}$. The black-dashed lines indicate the Borda-Carnot prediction.
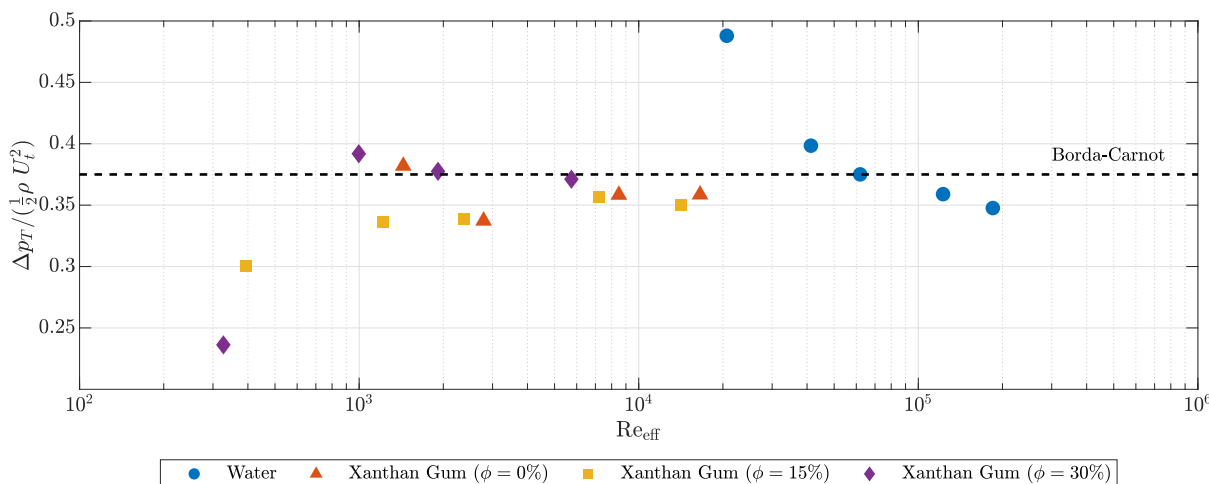


**Figure 4.** Ultimate pressure recovery coefficient ($\Delta p_T/(0.5\rho U_t^2)$) for all tested cases. All cases are plotted against their effective Reynolds number, while the markers indicate different fluid types. The Borda-Carnot prediction is indicated by the dashed line. The total pressure recovery coefficient demonstrate no discernible trend with effective Reynolds number of fluid type, but are consistently within 10% of the Borda-Carnot prediction.

tion of the sonic signal, which ultimately reduces signal-to-noise ratio, making it difficult to image deep into the pipe. This is clear when comparing the speckle images of water and XGΦ0% to those for XGΦ15% and XGΦ30%. The tracer particles appear smeared in the streamwise direction, offer less contrast relative to the background, and reduce in quantity as one travels deeper into the pipe. Despite this reduction in image quality, the images for XGΦ15% provide sufficient coherence to extract velocity vectors near the pipe wall, which could be used to determine the reattachment point. The images for XGΦ30% were ultimately too incoherent to extract any meaningful data, which speaks to the limitation of tilted plane wave UIV measuring in particle-laden flows with very large volume fractions.
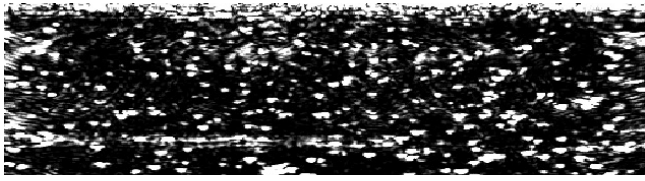


(a) Water
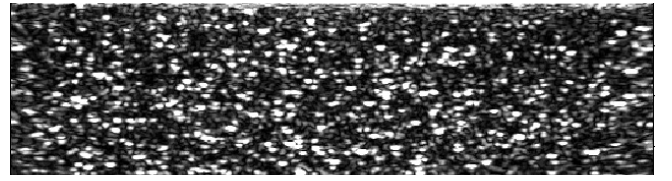


(b) Xanthum Gum (Φ = 0%)
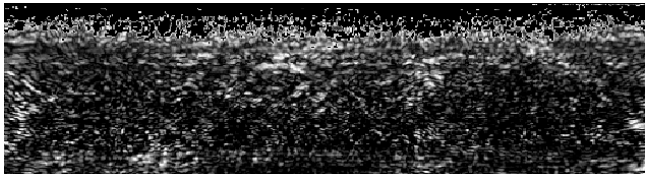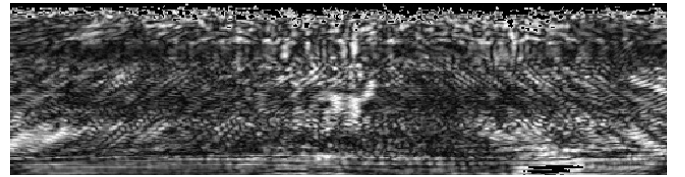


(c) Xanthum Gum (Φ = 15%)



(d) Xanthum Gum (Φ = 30%)

**Figure 5.** Typical ultrasound-rendered images taken near the pipe wall and downstream of the expansion for flows with (a) water (b) XGΦ0%, (b) XGΦ15% and (b) XGΦ30%.

Significant success in extracting flow fields from similar ultrasound-rendered images has been had in previous experiments. Fig. 6 presents the typical image-processing procedure used to prepare ultrasound-rendered images for flow-field extraction. A typical raw image generated by the ultrasound probe is shown in Fig. 6(a). To reduce noise within the images, a time-averaged image is subtracted from the raw images, resulting in images like that shown in Fig. 6(b). Additional post-processing measures are then taken, such as locally normalizing the intensity of the image to mitigate non-uniform brightness, as well as masking. These final images are then processed in DaVis 11, generating two-dimensional flow fields such as that presented in Fig. 6(d). The reader is referred to Najjari et al. (2021) for further details regarding the image-processing procedure.

Fig. 7(a) and (b) present mean streamwise-velocity fields ($u$) downstream of the throat with a velocity of $U_t = 0.51$m/s for single-phase water and XGΦ0% , respectively. Streamlines have been superimposed to reveal the mean flow. The streamwise ($x$) and spanwise ($y$) dimensions are normalized by the throat diameter, while the streamwise velocity is normalized by the velocity at the throat. The throat is located at $x = 0$, and the central axis of the pipe is located at $y = 1$. The streamline topology for pure water indicates a compact recirculation region and a reattachment length of roughly four throat diameters ($x/d \approx 4$). The result agrees with observations (Agarwal,

1994; Back & Roschke, 1972) and theory (Vanierschot & Van den Bulck, 2008) at similar Reynolds numbers. In comparison, the streamline topology for the xanthum-gum solution indicate an elongated recirculation region, as well as a reattachment length that occurs beyond the field-of-view.

The elongated reattachment length for the xanthum-gum solution could be attributed to two causes. The first possibility is a stable, laminar shear layer typically observed at low Reynolds numbers. Based on visualizations, Back & Roschke (1972) observed that the reattachment length grows with Reynolds number when Re $\sim$ O$(10^1)$, as increasing the flow's momentum essentially convects the shear layer further downstream. The growth reaches a maximum at approximately Re $\sim$ O$(10^2)$, at which point an instability develops within the shear layer causing it to undulate and reattach to the wall sooner. The strength of this instability grows with Reynolds number, thereby reducing the reattachment length when the Reynolds number grows between O$(10^2)$ and O$(10^3)$, after which the flow becomes self-similar and the reattachment point stays stationary. The Re$_{\text{eff}}$ of the xanthum-gum solution is sufficiently low that is to be expected that the reattachment length would exceed that which occurs within the self-similar turbulent regime.

On the other hand, the delayed reattachment length could also be caused by the anisotropic behaviour of the xanthum-gum solution, which attenuates turbulent disturbances in stream-normal (i.e. radial) direction. This correlation, which is characteristic of turbulent shear layers forming within shear-thinning fluids, between an elongated recirculation region and attenuated stream-normal disturbances has been observed by Pak et al. (1990), Castro & Pinho (1995), and Pereira & Pinho (2000a). The tendency of shear-thinning fluids to attenuate stream-normal disturbances has been attributed to the viscous relaxation of the fluid in the streamwise direction, resulting in the accentuation of streamwise turbulence, the attenuation of of turbulence in other directions, and ultimately the stabilization of the shear layer which delays reattachment. However, this anisotropic effect has typically been observed when Re$_{\text{eff}}$ $\sim$ O$(10^4)$, making it the less likely cause here. It should be mentioned that Pereira & Pinho (2000b) observed a shorter reattachment length for shear-thinning fluids relative to Newtonian fluids. They attributed their observation to a greater



| Raw images | Subtracting time average | Postprocessing | UIV |
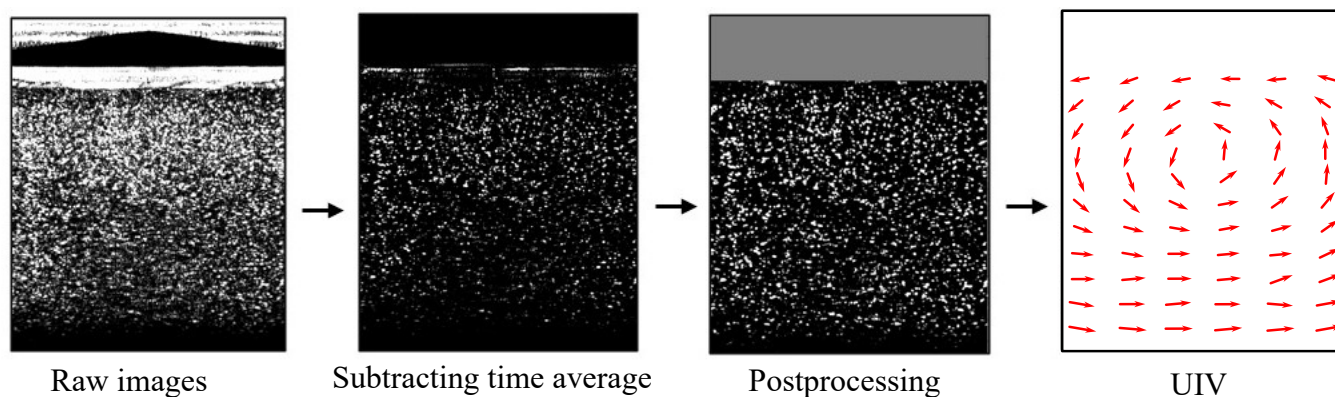
**Figure 6.** Typical image-processing procedure performed to prepare ultrasound-rendered images for flow field extraction.
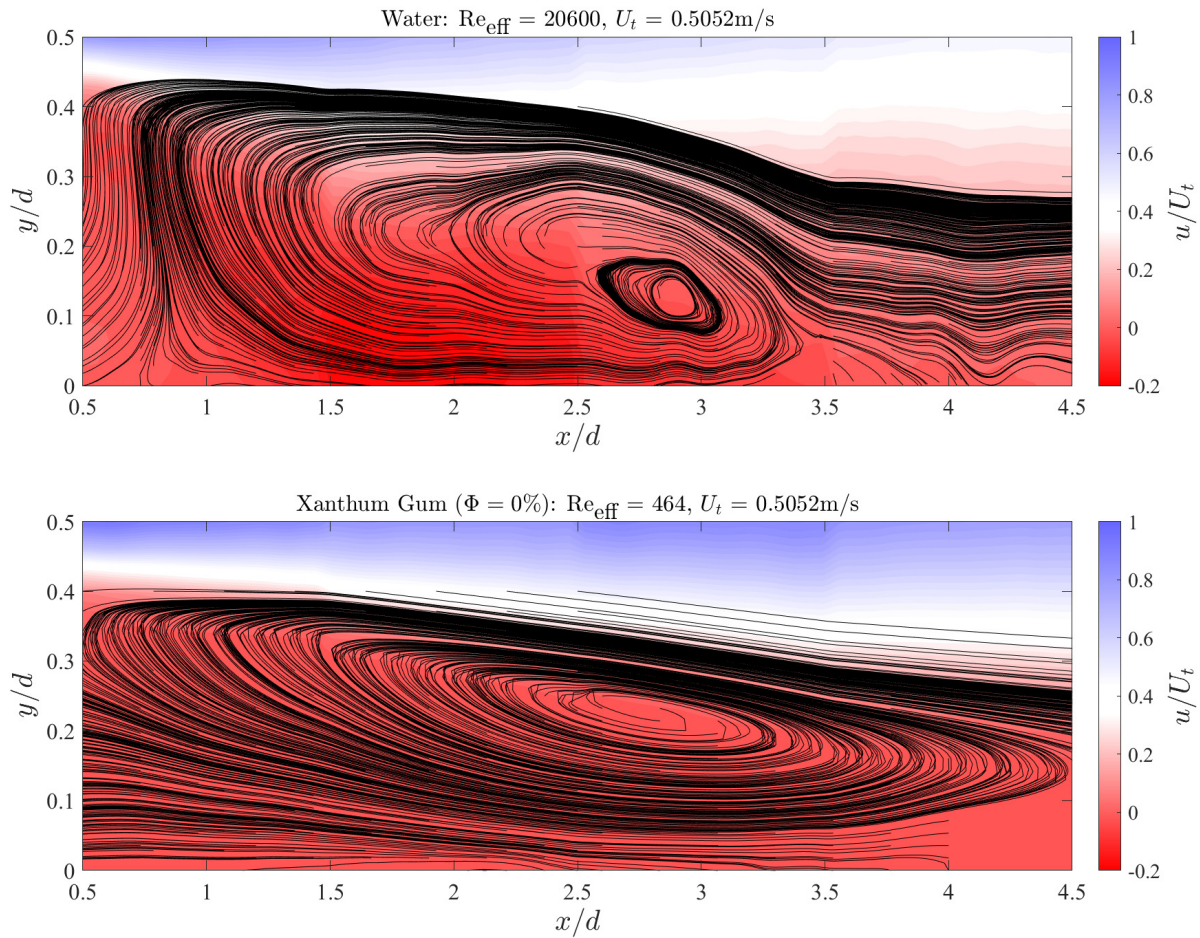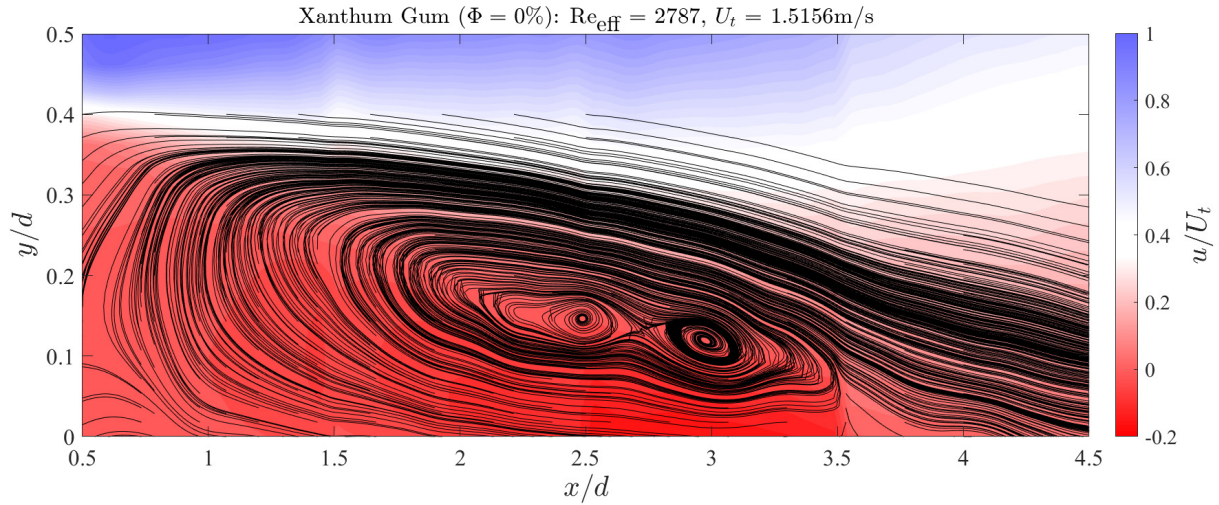
**Figure 7.** Fields of streamwise velocity normalized by the throat velocity ($u/U_t$) for single-phase water and xantham-gum solution, with streamlines overlaid to highlight the recirculation region and reattachment. Both fluids have a throat velocity of 0.5052m/s, which results in an effective Reynolds number of 464 and 20600 for the xanthum-gum solution and water, respectively. Streamlines would indicate a reattachment length of four throat diameters for water. The reattachment length for the xanthum-gum solution extends beyond the measured domain, but based on measured streamlines, would likely occur around 5.5 diameters.

level of turbulence prior to the expansion in comparison to other experiments, which was accentuated by the shear-thinning fluid upon passing through the throat resulting in a quicker reattachment.

Fig. 8 presents similar results as Fig. 7, but for XGΦ0% with a throat velocity $U_t = 1.52$m/s. Here the streamline topology indicates a reattachment of length of $x/d = 4$, which more closely resembles the reattachment length of water in Fig. 7 than that of the pure xanthum-gum solution. Similar results have been observed in Pak et al. (1990), Castro & Pinho (1995), and Pereira & Pinho (2000b), all of which have reported shear-thinning fluids exhibiting a reattachment length equal to or slightly smaller than that of a Newtonian fluid when $\mathrm{Re}_{\mathrm{eff}} \sim \mathrm{O}(10^3)$.

As previously stated, the signal attenuation through the tested dense suspensions caused primar-

**Figure 8.** Fields of streamwise velocity normalized by the throat velocity ($u/U_t$) for xantham-gum solution, with streamlines overlaid to highlight the recirculation region and reattachment. Fluid flows through the throat at 1.512m/s, which results in an effective Reynolds number of 2787. Streamlines would indicate a reattachment length of approximately $x/d \approx 4.5$.

ily by air pockets made it impossible to resolve flow fields. However, the signal-to-noise ratio along the pipe wall was low enough to extract velocity vectors whose sign could be used to identify the reattachment length. The lower and upper graphs of Fig. 9 present the streamwise velocity normalized by the maximum streamwise-velocity magnitude measured along the pipe for throat velocities of $U_t = 0.51$m/s and $1.52$m/s, respectively. If the water and XGΦ0% cases are considered, it is observed that water's velocity switches at roughly $x/d = 3.5$ for both velocities, whereas XGΦ0%'s velocity does not switch sign at the lower velocity, but does cross at $x/d = 3.5$ for the higher velocity. The result is consistent with the reattachment lengths identified through streamlines in Figs. 7 and 8, which speaks to the reliability of the method in accurately identifying the reattachment point in the absence of flow fields.

The dense suspension (XGΦ15%) exhibits effective Reynolds numbers that are comparable to the pure xanthum-gum solution when flowing at the same throat velocity. Furthermore, the the carrier fluid of the suspension is xanthum-gum solution. Given these two characteristics, one might presume that the dense suspension would present with a similar reattachment to that of the pure xanthum-gum solution, which could be attributed to a laminar shear layer that is further stabilized by the nature of the carrier fluid. This hypothesis would be supported by past experiments by Zhang & Rival (2023) and Barnes et al. (2024) on vortex rings forming within dense suspensions with a Newtonian carrier, which both observed the stabilization and diffusion of the shear layer and corresponding attenuation of the shear layer's instabilities. This previous work would then suggest that introducing a disperse phase would further promote the stabilization of the shear layer, which in turn would further elongate the recirculation region and delay reattachment. However, although the pipe-wall velocities for XGΦ0% and XGΦ15% do indicate a similar reattachment for the higher velocity case, they do not for the lower velocity case: XGΦ15% switches sign at

$x/d = 3.5$ while XG$\Phi$0% never exhibits a change in sign. The result runs contrary to expectations. One possible explanation might be that although the dense suspension might stabilize the shear layer and attenuate instabilities that would instigate reattachment, this is overcome by increased diffusion which mitigates the convective momentum of the shear layer thereby causing it to reattach quickly to the wall. It is cautioned that this hypothesis is based on single vectors along the pipe wall. A more capable measurement technique must be selected that allows for more reliable data to be collected for these onerous dense-suspension flows.
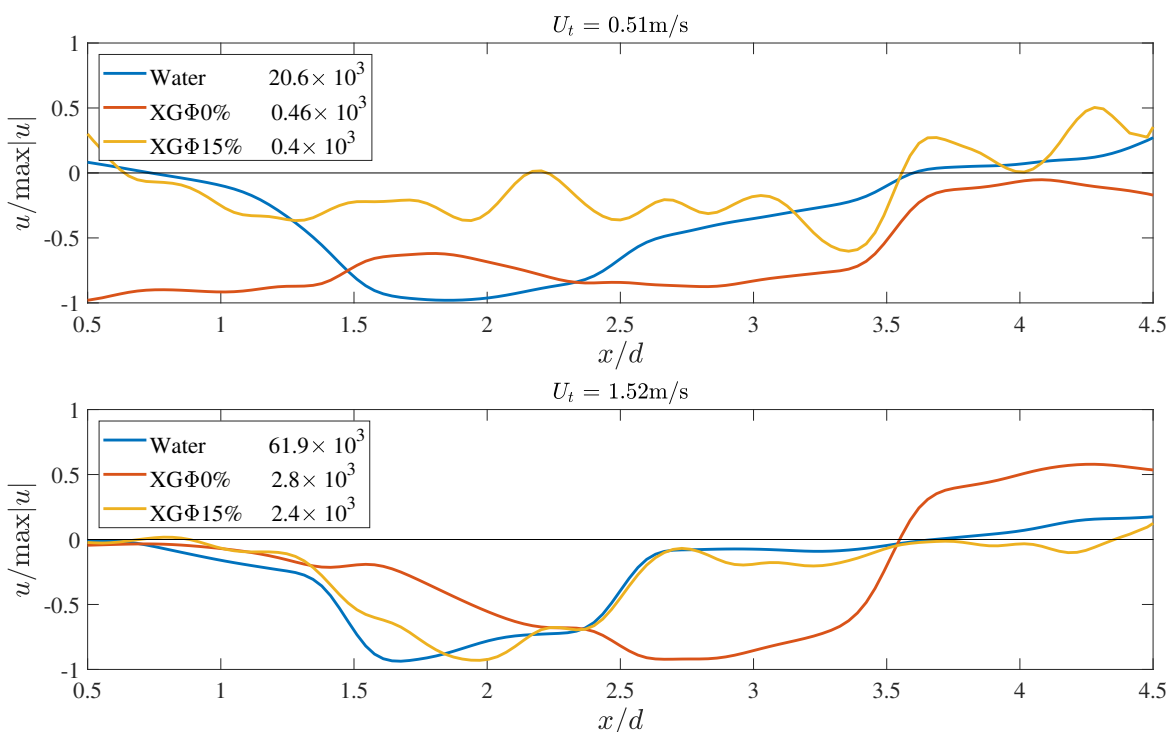


**Figure 9.** Streamwise velocity along the pipe wall normalized by the maximum pipe-wall streamwise-velocity magnitude for (upper) $U_t = 0.51$m/s and (lower) 1.52m/s. Effective Reynolds numbers are provided for each fluid case within the legend. The point where the pipe-wall velocity transitions from negative to positive gives an indication of the reattachment length.

One potential method to better characterize flows involving the dense suspensions tested here is X-ray Particle Tracking Velocimetry (XPTV; see Aliseda & Heindel (2021)). Although XPTV presents with difficulties such as the disentanglement of the integral attenuation along a beam path and regulatory issues, it is not hindered by signal attenuation like in tilted plane wave UIV and has become increasingly more viable. XPTV has been recently used to track particles within a fluidized bed of nanoparticles (Chen et al., 2019), characterize flows through opaque porous media (Bultreys et al., 2022), as well as to study cavitation within a venturi nozzle (Ge et al., 2022). Although once limited to very small volumes, XPTV can now fully resolve flow fields with sizeable volumes with reasonable spatial and temporal resolutions (Parker et al., 2024; Chen et al., 2019). The results suggest that extremely onerous suspensions like the ones tested here are beyond the capabilities of tilted plane wave UIV, and that alternatives like XPTV should be explored.

## 5. Conclusions

Pressure-field and UIV measurements were taken downstream of a sudden expansion for four fluids: pure water, and three suspensions comprised of 1750 parts-per-million xanthum-gum-in-water solution mixed with insoluble non-reactive mineral micro-particles to achieve disperse-phase volume fractions of $\Phi = 0\%, 15\%$ and $30\%$. Throat velocities were varied for all four fluids between 0.5m/s to 4.5m/s, thereby exploring an effective Reynolds number range of $1 \times 10^3 \leq \mathrm{Re}_{\mathrm{eff}} \leq 185 \times 10^3$, depending on the fluid. Pressure measurements demonstrate that, despite the shear-thinning nature of the xanthum-gum solution, the introduction of the disperse phase, or the variation of the effective Reynolds number, the rate of the pressure recovery remains equal across all fluids and agrees with the Borda-Carnot prediction when normalized in the form: $\Delta p/(0.5\rho U_t^2)$.

UIV measurements reveal variations in the reattachment length not captured by the pressure-tap measurements. Measurements involving water exhibited a reattachment length of $x/d \approx 4$, which agrees with previous measurements performed by Agarwal (1994) and others. In contrast, the pure shear-thinning xanthum-gum solution exhibited a delayed reattachment length at lower Reynolds numbers. The result could be potentially caused by the shear layer being laminar, or by viscous relaxation in the streamwise direction, which in turn attenuates disturbances in the stream-normal direction that would otherwise lead to early reattachment. It was hypothesized that the 15% volume-fraction dense suspension would exhibit reattachment lengths that were either similar to or further delayed than the xanthum-gum solution, in part due to the carrier phase also being xanthum-gum solution, and based on previous work done by Zhang & Rival (2023) and Barnes et al. (2024) that showed the attenuation of shear-layer instabilities forming within dense suspensions. However, streamwise pipe-wall velocities indicated no such delay in reattachment for the dense suspension, which instead exhibited reattachment lengths similar to that of water. It is hypothesized that the early reattachment may be caused by a diffusion of the shear layer within the dense suspension, which mitigates the convective momentum of the shear layer and keeps it from travelling further downstream. However, more data is required to state this conclusively.

The dense suspensions tested herein proved too onerous to measure via tilted plane wave UIV, as the suspensions attenuated the ultrasound signal via trapped air bubbles. No meaningful data could be extracted from the 30% volume-fraction suspension via UIV, while only single vectors along the pipe wall could be extracted from the 15% volume-fraction suspension. Although the pipe-wall velocity proved sufficient in roughly identifying reattachment, entire velocity fields would have provided more reliable results. The study provides an indication of the limitations of UIV when measuring dense suspensions of higher volume fraction and with complex composition. Alternatives, such as XPTV, should be considered when faced with similarly challenging mixtures.

## Acknowledgements

## Nomenclature

| | |
|---|---|
| $d$ | Throat diameter of expansion [m] |
| $D$ | Pipe diameter of expansion [m] |
| $K$ | Power law coefficient [mPa $s^n$] |
| $n$ | Power law exponent [dimensionless] |
| $\Delta p$ | Difference between the downstream pressure and throat pressure [Pa] |
| $\Delta p_T$ | Total pressure difference between downstream and throat [Pa] |
| $\mathrm{Re}_{\mathrm{eff}}$ | Effective Reynolds number [dimensionless] |
| $U_t$ | Velocity at the throat [m/s] |
| $x$ | Streamwise distance from the throat [m] |
| $\beta$ | Diameter ratio ($d/D$) [dimensionless] |
| $\dot{\gamma}$ | Characteristic shear rate [$s^{-1}$] |
| $\mu_{\mathrm{eff}}$ | Effective viscosity [Pa s] |
| $\rho$ | Density [kg/m$^3$] |
| $\sigma$ | Static pressure coefficient [dimensionless] |
| $\Phi$ | Volume fraction of the disperse phase [dimensionless] |

## References

Agarwal, N. K. (1994, 06). Mean Separation and Reattachment in Turbulent Pipe Flow Due to an Orifice Plate. *Journal of Fluids Engineering, 116*(2), 373-376. Retrieved from `https://doi.org/10.1115/1.2910284` doi: 10.1115/1.2910284

Aliseda, A., & Heindel, T. J. (2021). X-ray flow visualization in multiphase flows [Journal Article]. *Annual Review of Fluid Mechanics, 53*(Volume 53, 2021), 543-567. Retrieved from `https://www.annualreviews.org/content/journals/10.1146/annurev-fluid-010719-060201` doi: https://doi.org/10.1146/annurev-fluid-010719-060201

Back, L. H., & Roschke, E. J. (1972, 09). Shear-Layer Flow Regimes and Wave Instabilities and Reattachment Lengths Downstream of an Abrupt Circular Channel Expansion. *Journal of Applied Mechanics, 39*(3), 677-681.

Barnes, M., Zhang, K., & Rival, D. (2024). Lagrangian study of entrainment for confined vortex rings in dense suspensions using echo-lpt. *Experiments in Fluids*, *65*(3), 1–15.

Brennen, C. E. (2005). Fundamentals of multiphase flow.

Bultreys, T., Van Offenwert, S., Goethals, W., Boone, M. N., Aelterman, J., & Cnudde, V. (2022). X-ray tomographic micro-particle velocimetry in porous media. *Physics of Fluids*, *34*(4).

Castro, O. S., & Pinho, F. T. (1995). Turbulent expansion flow of low molecular weight shear-thinning solutions. *Experiments in Fluids*, *20*, 42-55.

Chen, X., Zhong, W., & Heindel, T. J. (2019). Orientation of cylindrical particles in a fluidized bed based on stereo x-ray particle tracking velocimetry (xptv). *Chemical Engineering Science*, *203*, 104-112. Retrieved from `https://www.sciencedirect.com/science/article/pii/S0009250919303380` doi: https://doi.org/10.1016/j.ces.2019.03.067

Crapper, M., Bruce, T., & Gouble, C. (1998). Flow field visualization of sediment-laden flow using ultrasonic imaging. *Dynamics of Atmospheres and Oceans*, *31*, 233-245.

Deen, N. G., Westerweel, J., & Delnoij, E. (2002). Two-phase piv in bubbly flows: Status and trends. *Chemical Engineering & Technology*, *25*(1), 97-101. Retrieved from `https://onlinelibrary.wiley.com/doi/abs/10.1002/1521-4125%28200201%2925%3A1%3C97%3A%3AAID-CEAT97%3E3.0.CO%3B2-7` doi: https://doi.org/10.1002/1521-4125(200201)25:1<97::AID-CEAT97>3.0.CO;2-7

Elkins, C. J., & Alley, M. T. (2007). Magnetic resonance velocimetry: applications of magnetic resonance imaging in the measurement of fluid motion. *Experiments in Fluids*, *43*, 823–858.

Escudier, M. P., & Smith, S. (1999). Turbulent flow of newtonian and shear-thinning liquids through a sudden axisymmetric expansion. *Experiments in Fluids*, *27*, 427-434.

Ge, M., Sun, C., Zhang, X., Coutier-Delgosha, O., & Zhang, G. (2022). Synchrotron x-ray based particle image velocimetry to measure multiphase streamflow and densitometry. *Radiation Physics and Chemistry*, *200*, 110395. Retrieved from `https://www.sciencedirect.com/science/article/pii/S0969806X22004376` (The 15th International Symposium on Radiation Physics (ISRP15), 6 - 10 December, 2021,Sunway University, Malaysia) doi: https://doi.org/10.1016/j.radphyschem.2022.110395

Han, E., Zhao, L., Ha, N. V., Hsieh, S. T., Szyld, D. B., & Jaeger, H. M. (2019, 6). Dynamic jamming of dense suspensions under tilted impact. *Physical Review Fluids*, *4*, 1-17. doi: 10.1103/PhysRevFluids.4.063304

Kupsch, C., Feierabend, L., Nauber, R., Buttner, L., & Czarske, J. (2021, 3). Ultrasound super-resolution flow measurement of suspensions in narrow channels. *IEEE Transactions on Ultrasonics, Ferroelectrics, and Frequency Control*, *68*, 807-817. doi: 10.1109/TUFFC.2020.3007483

Mäkiharju, S. A., Dewanckele, J., Boone, M., Wagner, C., & Griesser, A. (2022). Tomographic x-ray particle tracking velocimetry: Proof-of-concept in a creeping flow. *Experiments in Fluids*, *63*, 1–12.

Najjari, M. R., Zhang, K., & Rival, D. E. (2021, 9). Capturing both carrier and disperse phases in dense suspensions using harmonic ultrasound imaging velocimetry. *Measurement Science and Technology*, *32*, 1-9. doi: 10.1088/1361-6501/abf679

Pak, B., Cho, Y. I., & Choi, S. U. (1990). Separation and reattachment of non-newtonian fluid flows in a sudden expansion pipe. *Journal of Non-Newtonian Fluid Mechanics*, *37*(2-3), 175–199.

Parker, J. T., Dreier, T., Nilsson, D., & Mäkiharju, S. A. (2024). In-lab x-ray particle velocimetry for multiphase flows: Design principles and demonstration of o (1 khz) xpv. *Flow Measurement and Instrumentation*, *96*, 102536.

Pedley, T., & Kessler, J. O. (1992). Hydrodynamic phenomena in suspensions of swimming microorganisms. *Annual Review of Fluid Mechanics*, *24*(1), 313–358.

Pereira, A., & Pinho, F. (2000a). Turbulent characteristics of shear-thinning fluids in recirculating flows. *Experiments in fluids*, *28*(3), 266–278.

Pereira, A., & Pinho, F. (2000b). Turbulent characteristics of shear-thinning fluids in recirculating flows. *Experiments in Fluids*, *28*, 266-278.

Poelma, C. (2016). Ultrasound imaging velocimetry: a review. *Experiment in Fluids*, *58*, 1-28.

Raihan, M. K., Li, D., Kummetz, A. J., Song, L., Yu, L., & Xuan, X. (2020, 05). Vortex trapping and separation of particles in shear thinning fluids. *Applied Physics Letters*, *116*(18), 183701. Retrieved from `https://doi.org/10.1063/5.0008833` doi: 10.1063/5.0008833

Tashiro, H., & Tomita, Y. (1984). Sudden expansion of gas-solid two-phase flow in vertical downward flow. *Bulletin of JSME*, *27*(232), 2160–2165.

Tashiro, H., & Tomita, Y. (1986). Influence of diameter ratio on a sudden expansion of a circular pipe in gas—solid two-phase flow. *Powder technology*, *48*(3), 227–231.

Vanierschot, M., & Van den Bulck, E. (2008). The influence of swirl on the reattachment length in an abrupt axisymmetric expansion. *International journal of heat and fluid flow*, *29*(1), 75–82.

Zhang, K., & Rival, D. E. (2018, 07). Experimental study of turbulence decay in dense suspensions using index-matched hydrogel particles. *Physics of Fluids*, *30*(7), 073301. Retrieved from `https://doi.org/10.1063/1.5031767` doi: 10.1063/1.5031767

Zhang, K., & Rival, D. E. (2023). Study of recirculating metallic suspensions using ultrasound image velocimetry. In (p. 1-7).